Computation of the transition from quantum wells to bulk exciton states of cuprous oxide using B-spline basis functions

Bachelor thesis of
Leon Kühner

September 09, 2022

Supervisor: Prof. Dr. Jörg Main

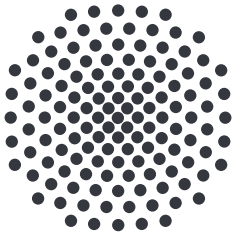

Institut für Theoretische Physik I
Universität Stuttgart
Pfaffenwaldring 57, 70550 Stuttgart

Contents

1 Introduction

Excitons first have been discovered in the 1930s by Frenkel and Wannier [1]. They are quasi particles that consist of an electron and an electron hole. Commonly, they occur in semiconductors like for example GaAs or Cu_2O. Due to the high Rydberg energies, excitons can be well detected experimentally in these materials. Of particular note is the detection of exciton states in Cu_2O up to a quantum number of $n = 25$ in the year 2014 by the Bayer group in Dortmund [2]. Since then a lot of research in excitons was done for example by Frank Schweiner [3] who introduced a Coulomb-Sturmian basis to solve the Schrödinger equation in bulk. In this thesis the excitons are in a quantum well and the band structure is neglected. Also another approach for calculating the energies, namely the B-splines basis functions, is investigated. They have been used for solving the Schrödinger equation since 1972 [4]. For the computational calculation an algorithm to solve the Schrödinger equation for excitons in quantum wells is implemented in Fortran. The aim of this thesis is to calculate the energy states of the exciton for different well widths. In addition, various potentials are used to compare the numerical calculations with analytical results and to approximate the Coulomb potential.

1.1 Structure of the thesis

In chapter 2 the theoretical basics are explained. There the structure of cuprous oxide and the basics to excitons are described. Further the eigenvalues for different potentials are analytically calculated. In chapter 3 the structure of the program that computes the problems numerically is outlined. Then in chapter 4 the results of the calculations are discussed. Firstly, the test of the convergence with different parameters is discussed. After that the numerical results for different analytical solvable problems are discussed. This serves the purpose of testing the program. In the end the computation of the transition from quantum wells to bulk exciton states are discussed. Here the numerical solutions are compared to the expected course.

2 Theoretical basics

Before the theory of excitons can be described, it is necessary to understand the solids in which they occur.

2.1 Structure of solids

In solid state materials, one differentiates between crystals and amorphous structures. Ideal crystals have a periodic structure while an ideal amorphous material has a disordered structure. Real solids have a structure that is in between. In the following, crystalline solids will be further discussed. Those have a periodic lattice and therefore every point in the lattice can be described by a translation vector

$$\boldsymbol{T} = n_1\boldsymbol{a} + n_2\boldsymbol{b} + n_3\boldsymbol{c}, \qquad n_i \in \mathbb{Z}, \tag{2.1}$$

where $\boldsymbol{a}$, $\boldsymbol{b}$, and $\boldsymbol{c}$ are the basis vectors of the coordinate system, that is specific for the crystal structure. The length of the basis vectors are called lattice constants. The lattice can be build by lining up unit cells. There are two types of unit cells. Those which contain only one lattice point and those which contain more lattice points. The former are called primitive unit cells and the latter non-primitive unit cells. The primitive unit cell fulfills the relation

$$U(\boldsymbol{r}) = U(\boldsymbol{r} + \boldsymbol{T}), \tag{2.2}$$

where U is a point in the lattice, $\boldsymbol{r}$ an arbitrary position vector and $\boldsymbol{T}$ the translation vector defined in equation (2.1). This means that the whole lattice can be described by a translation of the unit cell without overlap or void [5]. The different translations are classified by the Bravais lattice. In three dimensions 14 Bravais lattices exist. Besides the unit cell the overlap free and gapless decomposition of the space can be done with the so called Wigner-Seitz-cell. This cell contains only one lattice point, which is placed in the middle of the cell. Every point in the cell is closer to the lattice point of the cell than to every other lattice point [6]. Another description of the crystal is the so called reciprocal lattice. It can be defined with

$$\boldsymbol{G} = h\boldsymbol{a}^* + k\boldsymbol{b}^* + l\boldsymbol{c}^*, \qquad h, k, l \in \mathbb{N}, \tag{2.3}$$

where

$$\boldsymbol{a}^* = \frac{2\pi}{V_u} \cdot (\boldsymbol{b} \times \boldsymbol{c}), \tag{2.4}$$

$$\boldsymbol{b}^* = \frac{2\pi}{V_u} \cdot (\boldsymbol{c} \times \boldsymbol{a}), \tag{2.5}$$

$$\boldsymbol{c}^* = \frac{2\pi}{V_u} \cdot (\boldsymbol{a} \times \boldsymbol{b}), \tag{2.6}$$

are the primitive reciprocal translations. The volume V_u is the volume of the unit cell with $V_u = \boldsymbol{a} \cdot (\boldsymbol{b} \times \boldsymbol{c})$. The volume of the reciprocal cell therefore is $(2\pi)^3/V_u$. In the reciprocal lattice, a cell with maximal symmetry can be defined. This cell is called the first Brillouin zone, and corresponds to the Wigner-Seitz-cell in the primitive lattice [7].

2.2 Band structure

The conducting electrons in metals can be described in good approximation as a free electron gas in a constant potential with the potential barriers at the end of the solid. Because electrons are fermions the Pauli principle applies to them. Therefore the electrons are bound to the solid if the Fermi-energy E_f of the electron is lower than the constant potential V. The difference $V - E_f = \phi$ is the work that is needed to exit the material. However the cores also manipulate the potential so that the bottom of the potential becomes like the dashed potential in figure 2.1. In this periodic potential the electrons can be described by Bloch functions

$$\psi_{\boldsymbol{k}}(\boldsymbol{r}) = u_{\boldsymbol{k}}(\boldsymbol{r}) e^{i\boldsymbol{k}\cdot\boldsymbol{r}}, \tag{2.7}$$

where $u_{\boldsymbol{k}}(\boldsymbol{r})$ fulfills the condition

$$u_{\boldsymbol{k}}(\boldsymbol{r}) = u_{\boldsymbol{k}}(\boldsymbol{r} + \boldsymbol{G}). \tag{2.8}$$

For small amplitudes of the periodic potential the eigenvalues become

$$E_{\boldsymbol{k}} = E_{\boldsymbol{k}+\boldsymbol{G}} = \frac{\hbar^2}{2m} |\boldsymbol{k} + \boldsymbol{G}|^2 \tag{2.9}$$

in good approximation. These are parabolas in the reciprocal lattice. At the border of the Brillouin zone the parabolas intersect. Energy forbidden zones can arise for non-negligible amplitudes of the periodic potential. That means that no electron can have an energy state in this zone. In figure 2.2 the resulting energy dispersion schemes can be seen. This forms the band structure for solids with energy bands in which the electrons for

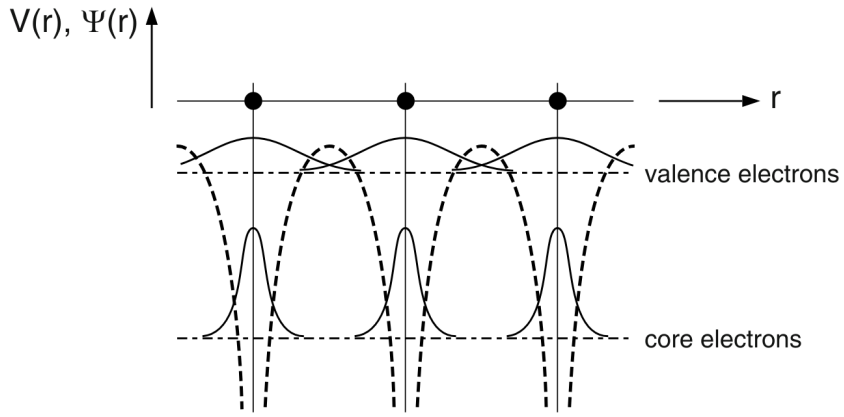

Figure 2.1: The potentials for the lattice points (dashed) with the wave functions of the core electrons and the valence electrons. Adapted from [9].

different orbitals lie. The wave function for core electrons and valence electrons can be seen in figure 2.1. The important bands for this thesis are the valence band which is the upper most band underneath the Fermi-energy and the conduction bands which are the bands over the Fermi-energy. For the description of the holes and electrons in the bands the Luttinger-Kohn model is used. This describes the electron and electron hole with effective masses [8].

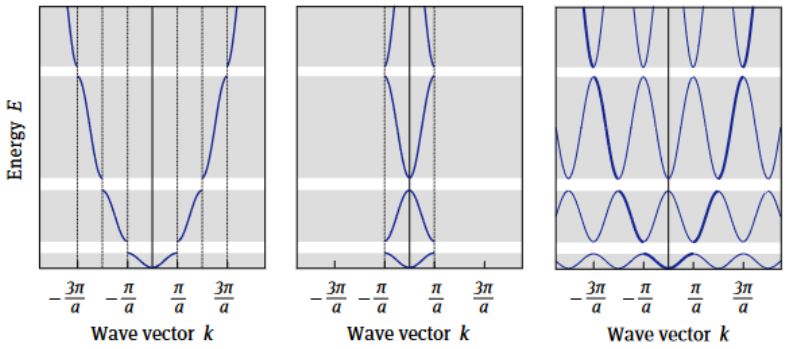

Figure 2.2: The energy dispersion curve for a one-dimensional lattice where the energy allowed zones are tinted gray and the energy forbidden zones are white. In the left figure the dispersion for one electron can be seen. In the middle figure the zone scheme is reduced to the Brillouin zone and on the right the periodic zone scheme is shown. Adapted from [9].

2.3 General theory of excitons

An exciton is a quasi particle that consist of an electron and an electron hole. It arises from a transition of the electron from the valence band to the conduction band. The bound states between the electron and the hole are called excitons. In the simplest model they can be described as a hydrogen-like quasi particle. Therefore the Hamiltonian reads

$$H = \frac{\boldsymbol{p}_\mathrm{e}^2}{2m_\mathrm{e}} + \frac{\boldsymbol{p}_\mathrm{h}^2}{2m_\mathrm{h}} - \frac{e^2}{4\pi\epsilon_0\epsilon|\boldsymbol{r}_\mathrm{e} - \boldsymbol{r}_\mathrm{h}|}, \tag{2.10}$$

where $\boldsymbol{p}$ is the three-dimensional momentum operator and the indices stand for electron and electron hole. The masses m_e and m_h are the effective masses of the electron and the electron hole in the solid. Further, ϵ_0 is the vacuum permeability and ϵ the dielectric constant. We assume that the valence band and conduction band are parabolic and have the band extrema at $\boldsymbol{k} = 0$. For cuprous oxide this is true for the conduction band but for the different valence bands correction terms are needed for an exact calculation. In this thesis the corrections are neglected. In the literature this Hamiltonian is often written with the material specific band gap energy E_g. We now introduce relative and center-of-mass coordinates to simplify the problem. This separates the motion of the center of mass and the motion of the electron and hole. Therefore we get

$$\boldsymbol{r} = \boldsymbol{r}_\mathrm{e} - \boldsymbol{r}_\mathrm{h}, \tag{2.11}$$

$$\boldsymbol{R} = (m_\mathrm{e}\boldsymbol{r}_\mathrm{e} + m_\mathrm{h}\boldsymbol{r}_\mathrm{h})/(m_\mathrm{e} + m_\mathrm{h}), \tag{2.12}$$

for the position of the center of mass $\boldsymbol{R}$ and the relative position $\boldsymbol{r}$ for the electron and hole. The momentum operators transform to

$$\boldsymbol{p} = (m_\mathrm{e}\boldsymbol{p}_\mathrm{e} - m_\mathrm{h}\boldsymbol{p}_\mathrm{h})/(m_\mathrm{e} + m_\mathrm{h}), \tag{2.13}$$

$$\boldsymbol{P} = \boldsymbol{p}_\mathrm{e} + \boldsymbol{p}_\mathrm{h}, \tag{2.14}$$

where $\boldsymbol{p}$ is the momentum for the relative motion and $\boldsymbol{P}$ is the momentum for the motion of the center of mass. The Hamiltonian now reads

$$H = \frac{\boldsymbol{p}^2}{2\mu} + \frac{\boldsymbol{P}^2}{2M} - \frac{e^2}{4\pi\epsilon_0\epsilon|\boldsymbol{r}|}, \tag{2.15}$$

with the reduced mass $\mu = m_\mathrm{e}m_\mathrm{h}/(m_\mathrm{e} + m_\mathrm{h})$ and the total mass $M = m_\mathrm{e} + m_\mathrm{h}$. For the hydrogen problem the Rydberg energy R_y is the lowest possible energy with the Bohr radius a_0. Since the masses are different, the Rydberg energy and radius needs to be adjusted to

$$R_\mathrm{exc} = R_y\frac{\mu}{m_0\epsilon^2}, \qquad a_\mathrm{exc} = a_0\frac{m_0\epsilon}{\mu}, \tag{2.16}$$

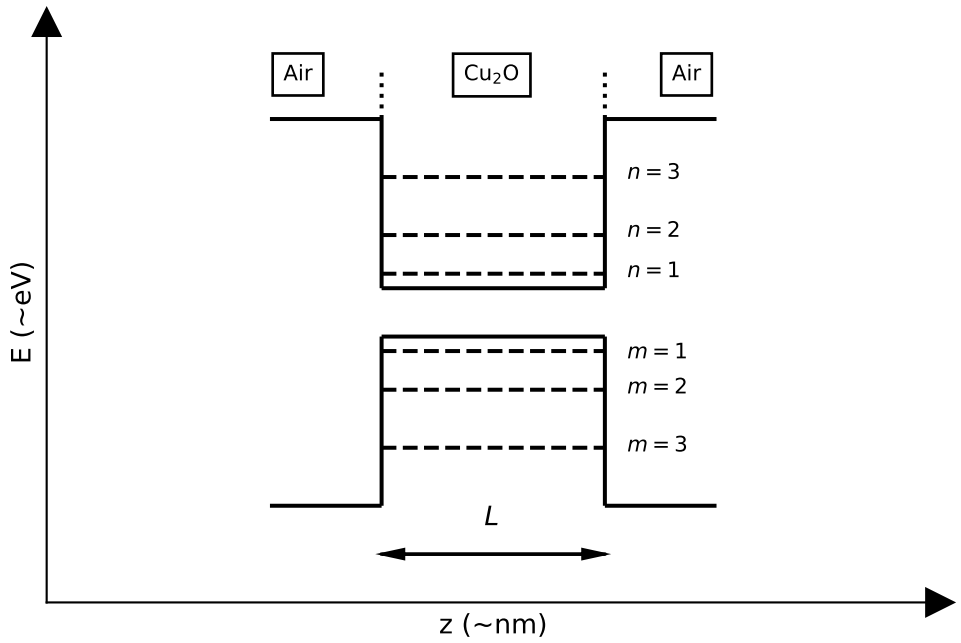

Figure 2.3: Schematic potential for the electron and the electron hole. The well width is about 0.1 to around 10 nm in this thesis. The eigenstates in the quantum well are marked with n for the electron and m and for electron hole, respectively.

with the dielectric constant ϵ and the reduced mass μ [3].

In this thesis we consider excitons in a cuprous oxide lattice with a confinement in z-direction with the length L. This can be represented by a quantum well, which affects the z component of the electron and the electron hole. We can separate the potential in a potential for the electron and one for the hole. The well barrier is equal to the work function energy of electrons in cuprous oxide to air (5.15 eV [10]) with the Rydberg binding energy (2.17 eV [10]) subtracted. The work function energy of electrons in cuprous oxide to air gives the energy that is needed to extract an electron from cuprous oxide. In figure 2.3 the schematic potential can be seen. The quantum well barrier is very high compared to the exciton Rydberg energy and can be approximated by an infinite quantum well. But we need to keep in mind that the highest energy in the quantum well

is 2.98 eV. The whole Hamiltonian for this problem reads

$$\begin{aligned} H =& \frac{\hbar^2}{2m_\mathrm{e}}\left(\frac{\partial^2}{\partial x_\mathrm{e}^2}+\frac{\partial^2}{\partial y_\mathrm{e}^2}+\frac{\partial^2}{\partial z_\mathrm{e}^2}\right)+\frac{\hbar^2}{2m_\mathrm{h}}\left(\frac{\partial^2}{\partial x_\mathrm{h}^2}+\frac{\partial^2}{\partial y_\mathrm{h}^2}+\frac{\partial^2}{\partial z_\mathrm{h}^2}\right) \\ & - \frac{e^2}{4\pi\epsilon_0\epsilon\sqrt{(x_\mathrm{e}-x_\mathrm{h})^2+(y_\mathrm{e}-y_\mathrm{h})^2+(z_\mathrm{e}-z_\mathrm{h})^2}} + V_\mathrm{e}(z_\mathrm{e}) + V_\mathrm{h}(z_\mathrm{h}). \end{aligned} \tag{2.17}$$

The use of the relative and center-of-mass coordinates brings the Hamiltonian to the shape of

$$H = \frac{\boldsymbol{p}^2}{2\mu}+\frac{\boldsymbol{P}^2}{2M}-\frac{e^2}{4\pi\epsilon_0\epsilon|\boldsymbol{r}|}+V_\mathrm{e}(z_\mathrm{e})+V_\mathrm{h}(z_\mathrm{h}). \tag{2.18}$$

Now cylindrical coordinates are used to simplify the Hamiltonian to

$$\begin{aligned} H =& \frac{\hbar^2}{2m_\mathrm{e}}\frac{\partial^2}{\partial z_\mathrm{e}^2}+\frac{\hbar^2}{2m_\mathrm{h}}\frac{\partial^2}{\partial z_\mathrm{h}^2}+\frac{\hbar^2}{2\mu}\left(\frac{\partial^2}{\partial\rho^2}-\frac{1}{\rho}\frac{\partial}{\partial\rho}+\frac{1}{\rho^2}\frac{\partial^2}{\partial\varphi^2}\right) \\ & - \frac{e^2}{4\pi\epsilon_0\epsilon\sqrt{\rho^2+(z_\mathrm{e}-z_\mathrm{h})^2}} + V_\mathrm{e}(z_\mathrm{e}) + V_\mathrm{h}(z_\mathrm{h}). \end{aligned} \tag{2.19}$$

The dimension of the Hamiltonian is now already reduced to four. For the eigenenergies the φ component only degenerates the energy $(2l+1)$-fold, where l is the quantum number of the φ-component. and for this reason is neglected for the calculations. This leaves a three-dimensional problem that only depends on the z positions of the electron and the hole and the distance between those in the xy-plane. Hence the Schrödinger equation for this problem is

$$H\psi(z_\mathrm{e}, z_\mathrm{h}, \rho) = E\psi(z_\mathrm{e}, z_\mathrm{h}, \rho) \qquad \text{with} \tag{2.20}$$

$$\begin{aligned} H =& \frac{\hbar^2}{2m_\mathrm{e}}\frac{\partial^2}{\partial z_\mathrm{e}^2}+\frac{\hbar^2}{2m_\mathrm{h}}\frac{\partial^2}{\partial z_\mathrm{h}^2}+\frac{\hbar^2}{2\mu}\left(\frac{\partial^2}{\partial\rho^2}-\frac{1}{\rho}\frac{\partial}{\partial\rho}+\frac{1}{\rho^2}\right) \\ & - \frac{e^2}{4\pi\epsilon_0\epsilon\sqrt{\rho^2+(z_\mathrm{e}-z_\mathrm{h})^2}} + V_\mathrm{e}(z_\mathrm{e}) + V_\mathrm{h}(z_\mathrm{h}). \end{aligned} \tag{2.21}$$

The boundary conditions for the differential equation are given by the potentials for the z-direction:

$$\begin{aligned} \psi(z_\mathrm{e}=0, z_\mathrm{h}, \rho) = 0, \quad \psi(z_\mathrm{e}=L, z_\mathrm{h}, \rho) = 0 \\ \psi(z_\mathrm{e}, z_\mathrm{h}=0, \rho) = 0, \quad \psi(z_\mathrm{e}, z_\mathrm{h}=L, \rho) = 0, \end{aligned} \tag{2.22}$$

because of the approximation of the infinitely high potential barriers. For the real well the effect of tunneling would give different boundary conditions. For the ρ-direction we demand that the wave function should vanish at infinity and at $\rho = 0$ due to the singularity in the Hamiltonian.

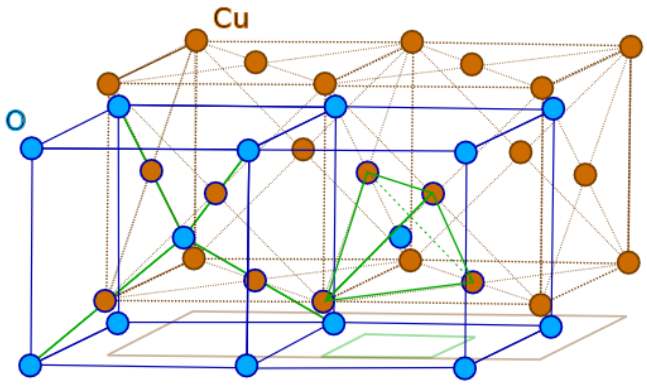

Figure 2.4: The bbc lattice of the (blue) oxygen ions and the fcc lattice of the (orange) copper ions together form the lattice of cuprous oxide. Taken from [11].

2.4 Cuprous oxide

Since the exciton states in cuprous oxide are investigated it is useful to take a closer look at cuprous oxide. The lattice contains of oxygen ions that form a bbc lattice and of copper ions that form an fcc lattice as can be seen in figure 2.4. The lattices are shifted to each other by 1/4 of the space diagonal [3]. The band-gap-energy of cuprous oxide is E_g =2.172 eV [2]. The electron bands can be seen in figure 2.5. The effective mass of the electron in the minimum of the Γ_6^+ band is $m_\mathrm{e} = 0.99 m_0$ [13] where m_0 is the electron mass in vacuum. For the valence band Γ_7^+ the effective mass for the hole is $m_\mathrm{h} = 0.69 m_0$ and for the Γ_8^+ band the effective mass is $m_\mathrm{h} = 0.58 m_0$ [13]. The dielectric constant for cuprous oxide is $\epsilon = 7.5$ at a temperature of T = 293 K [14]. With this information the green and yellow exciton states can be calculated as discussed in section 2.3. The exciton Rydberg energy for the light hole is $R_\mathrm{exc} = 88.46$ meV and for the heavy hole $R_\mathrm{exc} = 98.35$ meV. The exciton Bohr radius for the light hole is $a_\mathrm{exc} = 1.085$ nm and for the heavy hole the exciton Bohr radius is $a_\mathrm{exc} = 0.976$ nm. This is around 20 times as large as the Bohr radius.

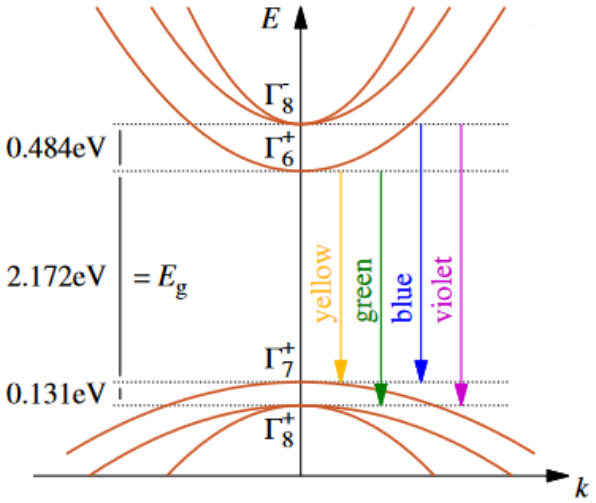

Figure 2.5: The conduction bands Γ_6^+ and Γ_8^- with the valence bands Γ_7^+ and Γ_8^+. The energy differences are given on the left and the colored arrows show the different exciton series which occur when the electron is in the according conduction band and the hole is in the according valence band. Taken from [12].

2.5 Calculations for different potentials

If we consider an exciton in a quantum well along the z-axis then we can think that for very small quantum wells the impact of the distance in z-direction becomes negligible. This reduces our Hamiltonian to a 2D hydrogen-like problem:

$$H = \frac{\hbar^2}{2m_\mathrm{e}}\frac{\partial^2}{\partial z_\mathrm{e}^2} + \frac{\hbar^2}{2m_\mathrm{h}}\frac{\partial^2}{\partial z_\mathrm{h}^2} + \frac{\hbar^2}{2\mu}\left(\frac{\partial^2}{\partial\rho^2} - \frac{1}{\rho}\frac{\partial}{\partial\rho} + \frac{1}{\rho^2}\right) - \frac{e^2}{4\pi\epsilon_0\epsilon\rho} + V_\mathrm{e}(z_\mathrm{e}) + V_\mathrm{h}(z_\mathrm{h}) \quad (2.23)$$

with

$$V_\mathrm{e}(z_\mathrm{e}) = \begin{cases} 0 & \text{for } |z_\mathrm{e}| < L/2 \\ \infty & \text{for } |z_\mathrm{e}| \geq L/2 \end{cases}$$

and

$$V_\mathrm{h}(z_\mathrm{h}) = \begin{cases} 0 & \text{for } |z_\mathrm{h}| < L/2 \\ \infty & \text{for } |z_\mathrm{h}| \geq L/2 \end{cases},$$

where L is the quantum well width. For this problem analytical solutions can be calculated because we can separate each variable and get analytical solvable differential equations. For the z-direction of the electron we get the Hamiltonian

$$H_{z_\mathrm{e}} = \frac{\hbar^2}{2m_\mathrm{e}}\frac{\partial^2}{\partial z_\mathrm{e}^2} + V_\mathrm{e}(z_\mathrm{e}). \quad (2.24)$$

We use the approach

$$\psi(z_\mathrm{e}) = A\sin(kz_\mathrm{e}) + B\cos(kz_\mathrm{e}), \quad (2.25)$$

where k is the wave number. Due to the potential we get the boundary conditions $\psi(L/2) = \psi(-L/2) = 0$. Now we plug this in our stationary Schrödinger equation

$$\left(\frac{\hbar^2}{2m_\mathrm{e}}\frac{\partial^2}{\partial z_\mathrm{e}^2} + V_\mathrm{e}(z_\mathrm{e})\right)\psi(z_\mathrm{e}) = E\psi(z_\mathrm{e}), \quad (2.26)$$

$$\frac{\hbar^2}{2m_\mathrm{e}}k^2\psi(z_\mathrm{e}) = E\psi(z_\mathrm{e}), \quad (2.27)$$

$$E = \frac{\hbar^2 k^2}{2m_\mathrm{e}}. \quad (2.28)$$

With the boundary conditions we know that A or B have to be zero. We get $k_n = n\pi/L$ and the eigenfunctions

$$\psi_n(z_\mathrm{e}) = \begin{cases} A\sin(k_n z_\mathrm{e}) & \text{for even } n \\ B\cos(k_n z_\mathrm{e}) & \text{for odd } n. \end{cases} \quad (2.29)$$

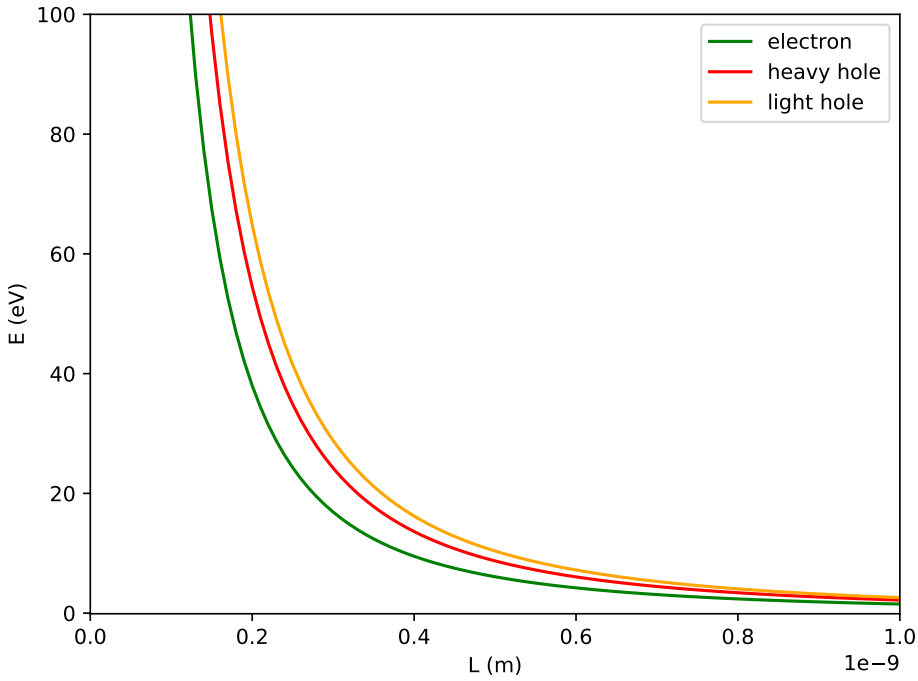

Figure 2.6: Lowest energy eigenvalue in an infinite quantum well over the width of the quantum well for the electron and the light and heavy hole.

With the normalisation we get $A = B = \sqrt{2/L}$. Therefore the searched eigenenergies are

$$E_n = \frac{\hbar^2 n^2 \pi^2}{2m_\mathrm{e} L^2}, \tag{2.30}$$

and can be seen in figure 2.6. This is analogous to the z_h dependent part which leaves us with the ρ dependent part. The Schrödinger equation reads

$$\left(\frac{\hbar^2}{2\mu}\left(\frac{\partial^2}{\partial\rho^2} - \frac{1}{\rho}\frac{\partial}{\partial\rho} + \frac{1}{\rho^2}\right) - \frac{e^2}{4\pi\epsilon_0\epsilon\rho}\right)\psi(\rho) = E\psi(\rho). \tag{2.31}$$

This corresponds to the two-dimensional hydrogen problem where we know the eigenenergies

$$E_j = -\frac{R_\mathrm{exc}}{(j+\frac{1}{2})^2}, \tag{2.32}$$

with the quantum numbers $j = 0, 1, 2, ...$, of ρ [15]. In the following the energy for $j = 0$ will be called 2D Rydberg energy. Therefore the total energy of an exciton becomes

$$E_{n,m,j} = \frac{\hbar^2 n^2 \pi^2}{2m_\mathrm{e} L^2} + \frac{\hbar^2 m^2 \pi^2}{2m_\mathrm{h} L^2} - \frac{R_\mathrm{exc}}{(j+\frac{1}{2})^2}, \tag{2.33}$$

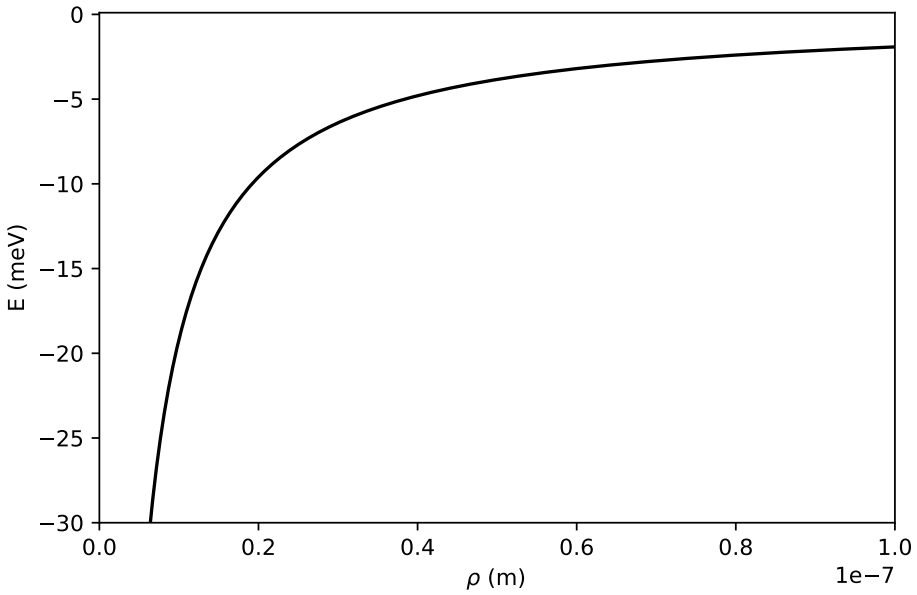

Figure 2.7: $1/\rho$-potential in the region from $\rho = 0$ to 100 nm.

where n and m are the quantum number of the energy in the electron or electron hole potential and j is the quantum number of the two-dimensional hydrogen problem. The potential can be seen in figure 2.7.

Another approach for an approximation of the Coulomb potential is an adiabatic potential. We assume that the motion in z-direction is very fast compared to the motion in ρ direction. So it is reasonable to average over the distance between the electron and hole regarding the z-axes. Hence we need to calculate the potential

$$\begin{aligned} V(\rho, L) &= -\frac{e^2}{4\pi\epsilon_0\epsilon}\frac{1}{L^2}\int_{-L/2}^{L/2}\int_{-L/2}^{L/2}\frac{1}{\sqrt{\rho^2+(z_\mathrm{e}-z_\mathrm{h})^2}}\mathrm{d}z_\mathrm{e}\mathrm{d}z_\mathrm{h} \\ &= -\frac{e^2}{4\pi\epsilon_0\epsilon}\frac{1}{L^2}\int_{-L/2}^{L/2}\operatorname{arcsinh}\left(\frac{2z_\mathrm{e}+L}{2\rho}\right)-\operatorname{arcsinh}\left(\frac{2z_\mathrm{e}-L}{2\rho}\right)\mathrm{d}z_\mathrm{e} \\ &= -\frac{e^2}{4\pi\epsilon_0\epsilon}\frac{1}{L^2}\left(2\rho+2L\operatorname{arcsinh}\left(\frac{L}{\rho}\right)-\sqrt{4\rho^2+4L^2}\right). \end{aligned} \tag{2.34}$$

This way the potential only depends on ρ and the widths of the quantum well L. This potential converges to the $1/\rho$ potential for large ρ. For small well widths L the adiabatic potential also converges to the $1/\rho$-potential. In figure 2.8 the adiabatic potential is shown for different well widths L. The $1/\rho$-potential would be indistinguishable from the

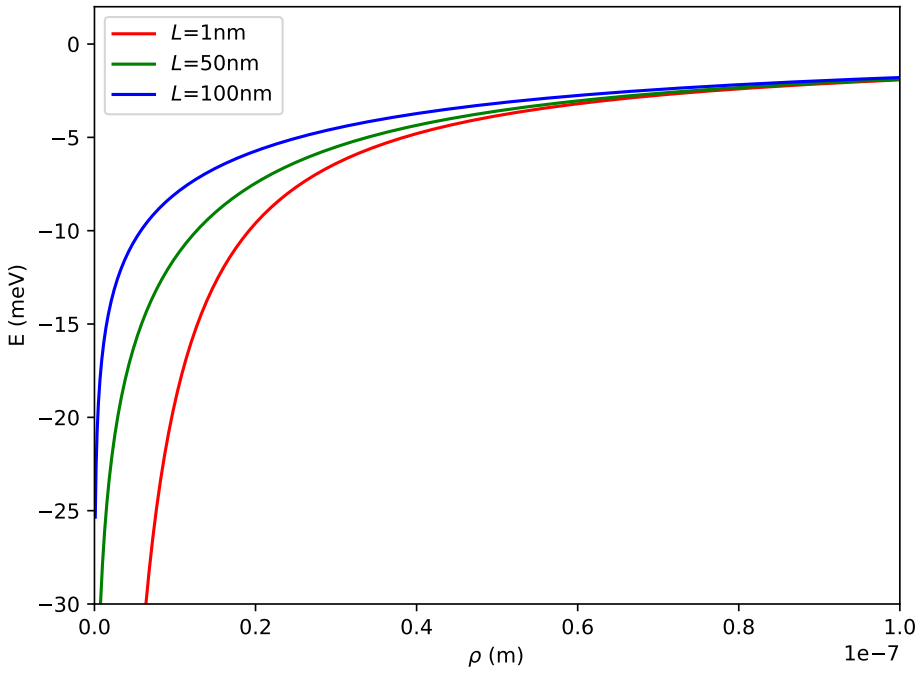

Figure 2.8: Adiabatic potential for different quantum well widths L as a function of ρ.

$L = 1\,\mathrm{nm}$ line in this plot and has therefore been omitted.

Obviously there is also the option to fully neglect the attractive potential. This way we can test the program for each dimension. The problem is also analytically solvable. Therefore we can compare the results of the program with the analytical solution. The parts of the Hamiltonian which depend on z_e and z_h have been solved already with equation (2.30). So we are left with

$$H_\rho = \frac{\hbar^2}{2\mu}\left(\frac{\partial^2}{\partial\rho^2} - \frac{1}{\rho}\frac{\partial}{\partial\rho} + \frac{1}{\rho^2}\right), \tag{2.35}$$

and the differential equation

$$\frac{\hbar^2}{2\mu}\left(\frac{\partial^2}{\partial\rho^2} - \frac{1}{\rho}\frac{\partial}{\partial\rho} + \frac{1}{\rho^2}\right)\psi(\rho) = E\psi(\rho). \tag{2.36}$$

This can be written as

$$\left(\frac{\partial^2}{\partial\rho^2} - \frac{1}{\rho}\frac{\partial}{\partial\rho} + \frac{1}{\rho^2} - \frac{2\mu E}{\hbar^2}\right)\psi(\rho) = 0 \tag{2.37}$$

For this kind of problem the solution is given by the Bessel functions $J_n(\rho)$. To calculate the eigenvalues the Bessel function needs to vanish at the boundary condition. We also have the boundary condition $\psi(\rho = R) = 0$ because we cannot let ρ go to infinity due to the nature of computers. This leads to the energies

$$E_{n,m,j} = \frac{\hbar^2 n^2 \pi^2}{2m_e L^2} + \frac{\hbar^2 m^2 \pi^2}{2m_h L^2} + \frac{\hbar^2 \rho_j}{2\mu R^2}, \tag{2.38}$$

where $J_0(\rho_j) = 0$ is the j-th root of the first Bessel function.

2.6 B-splines

A spline is defined as a curve $\boldsymbol{s}(u)$ of degree n with knots $a_0, ..., a_m$, where $a_i \leq a_{i+1}$ and $a_i < a_{i+n+1}$ is true for all possible i, and $\boldsymbol{s}(u)$ is $n - r$ times differentiable at any r-fold knot, and $\boldsymbol{s}(u)$ is a polynomial of degree $\leq n$ over each knot interval $[a_i, a_{i+1}]$, for $i = 0, ..., m - 1$. The knots are called r-fold knots if $a_i < a_{i+1} \leq, ..., a_{i+r} < a_{i+r+1}$. These splines can be represented by using so called B-splines $B_i^n(u)$ with minimal support and control points $\boldsymbol{c}_i$. The B-splines also need certain continuity properties. In this basis a spline $\boldsymbol{s}(u)$ becomes

$$\boldsymbol{s}(u) = \sum \boldsymbol{c}_i B_i^n(u). \tag{2.39}$$

The B-splines can be calculated recursively by the Cox-de Boor recursion formula. For a sequence of knots a_i with increasing a_i

$$B_i^0(u) = \begin{cases} 1 & \text{if } u \in [a_i, a_{i+1}) \\ 0 & \text{otherwise} \end{cases}$$

and

$$B_i^n(u) = \alpha_i^{n-1} B_i^{n-1}(u) + (1 - \alpha_{i+1}^{n-1}) B_{i+1}^{n-1}(u) \tag{2.40}$$

with the local parameter

$$\alpha_i^{n-1} = \frac{u - a_i}{a_{i+n} - a_i}, \tag{2.41}$$

to the support of $B_i^n(u)$. B-splines are zero outside the knot sequence. The end points can be controlled by inserting n-fold knots. For a B-spline with degree n the end points then become the same as the control points. This way the continuity properties are

managed. At each knot the first $(n-r)$-th derivatives of $\boldsymbol{s}(u)$ are continuous at the r-th fold knot a_i. For a single B-spline the derivative can be calculated with

$$\frac{d}{du}B_i^n(u) = \frac{u}{u_{i+n} - u_i}B_i^{n-1}(u) - \frac{u}{u_{i+n+1} - u_{i+1}}B_{i+1}^{n-1}(u). \tag{2.42}$$

B-splines are used to approximate wave functions or to interpolate curves [16]. Instead of calculating $\boldsymbol{s}(u)$ for the numerical calculation, an equivalent recursion formula is calculated. This is more efficient than using the Cox-de Boor recursion formula. For this a new set of control points $\boldsymbol{d}_i^r$ with $\boldsymbol{d}_i^0 = \boldsymbol{c_i}$ for $i = (k-r), ..., k$ is introduced. The recursion formula reads

$$\boldsymbol{d}_i^r = \left(1 - \alpha_i^r \boldsymbol{d}_{i-1}^{r-1}\right) + \alpha_i^r \boldsymbol{d}_i^{r-1} \tag{2.43}$$

for $r = 1, ..., n$ and $i = k - n + 1 + r, ..., k$ with the coefficients

$$\alpha_i^r = \frac{u_a i}{a_{i+n-r} - a_i}. \tag{2.44}$$

The result for this recursion is $\boldsymbol{s}(u) = \boldsymbol{d}_k^{n-1}$. In this formula only coefficients that are not zero are calculated [17].

3 Numerical calculation

For the computation of the problem discussed in section 2.3, an algorithm of Pavel Belov [18] is implemented in Fortran. The advantage of Fortran is the huge amount of optimised routines for mathematical operations. This program uses B-spline basis functions to calculate the wave-functions and the eigenvalues. The in section 2.5 discussed potentials are added, so one can switch between those potentials. The boundary conditions are implemented by adding ghost knots at these points. So for the boundary condition $\psi(z_\mathrm{e} = 0) = 0$ as many knots as the order of the B-splines are implemented at $z_\mathrm{e} = 0$. These knots are added automatically by the program. The boundary conditions are given by equation (2.22)

$$\begin{aligned} \psi(z_\mathrm{e} = 0) &= 0, \qquad & \psi(z_\mathrm{e} = L) &= 0, \\ \psi(z_\mathrm{h} = 0) &= 0, \qquad & \psi(z_\mathrm{h} = L) &= 0, \\ \psi(\rho = 0) &= 0, \qquad & \psi(\rho \to \infty) &= 0. \end{aligned}$$

Since this is a numerical calculation instead of $\psi(\rho \to \infty) = 0$ a large boundary condition $\rho = \rho_\mathrm{max}$ is used which can be manually set. The number of knots for the B-splines can be manually set. In the z_e- and z_h-direction the knots are equidistant. For the knot sequence in ρ-direction the position for the i-th knot is calculated by

$$\rho_i = \left(\frac{i - \mathrm{kord}}{n_\rho - 1} \right)^3 \rho_\mathrm{max}, \tag{3.1}$$

where kord is the order of the B-splines, n_ρ is the set number of knots in ρ-direction and ρ_max is the point on which the B-splines in ρ-direction become zero. This is useful because the B-splines need more knots close to zero than for $\rho \to \rho_\mathrm{max}$, so one can have a better resolution of the function close to zero.

The B-splines B are calculated and multiplied with the Hamiltonian H, the matrix M reads as

$$\begin{aligned} M &= \langle B | \, H \, | B \rangle \\ &= \int\int\int B(z_\mathrm{e}) B(z_\mathrm{h}) B(\rho) H B(z_\mathrm{e}) B(z_\mathrm{h}) B(\rho) \mathrm{d}z_\mathrm{e} \mathrm{d}z_\mathrm{h} \mathrm{d}\rho \end{aligned} \tag{3.2}$$

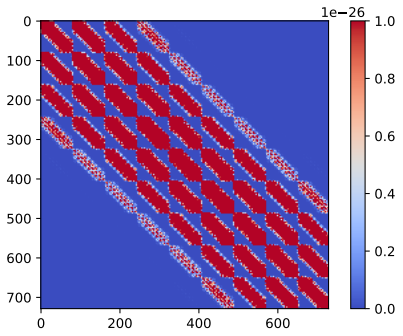

Figure 3.1: The banded structure of the matrix M when the innermost for-loop is over the knots in ρ -direction. Every pixel represents an entry with its absolute value.

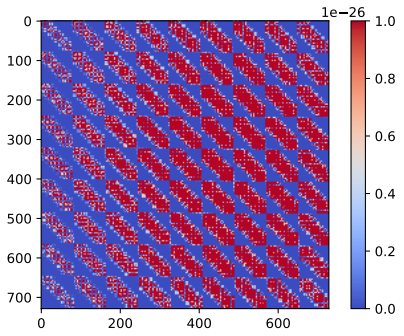

Figure 3.2: The banded structure of the matrix M when the outermost for-loop is over the knots in ρ -direction. Every pixel represents an entry with its absolute value.

which is a matrix with $(n_{z_\mathrm{e}} + n_{z_\mathrm{h}} + n_{z_\rho} + 6\mathrm{k}_\mathrm{ord} - 6)^2$ entries. It can be seen that for the computation time the order of the B-splines should be as low as possible. However for the quality of the calculations the order of the B-splines should be as high as possible. For the calculations B-splines up to the fifth order were chosen, since there are second derivatives in the matrix and it was assumed that a polynomial of the order three can describe the wave function sufficiently. The matrix M is calculated line by line over three for-loops where the outer loops are over the number of knots in the z-directions and the inner loop is over the knots in ρ-direction. This is important because it influences the banded structure of the matrix as can be see for a small matrix in figure 3.1 and figure 3.2. There it can be seen that when the innermost for-loop goes over the knots in ρ -direction, the bandwidth is smaller. This can be exploited by using different algorithms for the computation of the eigenvalues. However this is not yet done. Firstly, the integrals

$$
\begin{aligned}
B_{\mathrm{e},i} &:= \int_{z_{e,i}}^{z_{e,i+1}} B(z_\mathrm{e})\mathrm{d}z_\mathrm{e}, \\
B_{\mathrm{h},j} &:= \int_{z_{h,j}}^{z_{h,j+1}} B(z_\mathrm{h})\mathrm{d}z_\mathrm{h}, \\
B_{\rho,l} &:= \int_{\rho_l}^{\rho_{l+1}} B(\rho)\mathrm{d}\rho,
\end{aligned}
$$

are calculated with the knots $z_{e,i}, z_{h,j}$ and ρ_l with $i = 1, ..., n_{z_\mathrm{e}}$, $j = 1, ..., n_{z_\mathrm{h}}$ and $l = 1, ..., n_\rho$. Also k is the k-th line of the matrix M with $k = 1, ..., n_{z_\mathrm{e}} n_{z_\mathrm{h}} n_\rho$ as they occur several times for each matrix entry. In the next step the entry $M(k, m)$ is calculated,

where $m = (i-1)n_{z_\mathrm{h}} n_\rho + (j-1)n_\rho + l$. The calculation reads

$$
\begin{aligned}
M(k,m) =& \frac{\hbar^2}{2m_\mathrm{e}} \left(\int_{z_{e,i}}^{z_{e,i+1}} B(z_\mathrm{e}) \frac{\mathrm{d}^2}{\mathrm{d}z_\mathrm{e}^2} B(z_\mathrm{e}) \right) B_{\mathrm{h},j} B_{\rho,l} \\
&+ \frac{\hbar^2}{2m_\mathrm{h}} \left(\int_{z_{h,j}}^{z_{h,j+1}} B(z_\mathrm{h}) \frac{\mathrm{d}^2}{\mathrm{d}z_\mathrm{e}^2} B(z_\mathrm{h}) \right) B_{\mathrm{e},i} B_{\rho,l} \\
&+ \frac{\hbar^2}{2\mu} \left(\int_{\rho_l}^{\rho_{l+1}} B(\rho) \frac{\mathrm{d}^2}{\mathrm{d}\rho^2} B(\rho) \right) B_{\mathrm{e},i} B_{\mathrm{h},j} \\
&- \frac{\hbar^2}{2\mu} \left(\int_{\rho_l}^{\rho_{l+1}} \frac{B(\rho)}{\rho} \frac{\mathrm{d}}{\mathrm{d}\rho} B(\rho) \right) B_{\mathrm{e},i} B_{\mathrm{h},j} \\
&+ \frac{\hbar^2}{2\mu} \left(\int_{\rho_l}^{\rho_{l+1}} \frac{B(\rho) 2}{\rho^2} \right) B_{\mathrm{e},i} B_{\mathrm{h},j} \\
&+ \left(\int_{z_{e,i}}^{z_{e,i+1}} B(z_\mathrm{e}) V(z_\mathrm{e}) B(z_\mathrm{e}) \right) B_{\mathrm{h},j} B_{\rho,l} \\
&+ \left(\int_{z_{h,j}}^{z_{h,j+1}} B(z_\mathrm{h}) V(z_\mathrm{h}) B(z_\mathrm{h}) \right) B_{\mathrm{e},i} B_{\rho,l} \\
&- \left(\int_{z_{e,i}}^{z_{e,i+1}} \int_{z_{h,j}}^{z_{h,j+1}} \int_{\rho_l}^{\rho_{l+1}} B(z_\mathrm{e}, z_\mathrm{h}, \rho)^2 \frac{e^2}{4\pi\epsilon_0 \epsilon \sqrt{\rho^2 + (z_\mathrm{e} - z_\mathrm{h})^2}} \right).
\end{aligned}
\tag{3.3}
$$

This step is fully parallelized and therefore the computation time is inversely proportional to the number of cores which are involved. In the next step the inverse of the B-spline matrix is calculated using routines from the LAPACK [19]. This inverse is multiplied from the left to matrix M. From this matrix product the eigenvalues are calculated also using routines from LAPACK. The banded structure of the matrix benefits the eigenvalue calculation. In the last step the eigenvalues are sorted according to their value.

4 Results and discussion

In the following, excitons with a heavy hole (except for the calculations for figure 4.12) in a quantum well with width $L = \Delta$ are considered. Besides this physical parameters, the numerical parameters like the number of knots and the numerical boundary condition are discussed.

4.1 Test of convergence

Before the computation of the transition from quantum wells to bulk exciton states can be done, it is useful to test the convergence of the numerical implementation. On the one hand we want exact solutions for the energy states but on the other hand a short computation time. Therefore it is necessary to compare results of the program with analytical results, so the accuracy of the results can be determined. For this the analytical solutions of chapter 2 are used. The parameters that can be varied are the number of knots in each direction, the widths of the quantum wells and the order of the B-splines. In the first test the parameter for the number of knots in ρ-direction is examined. In figure 4.1 the first twelve numerically solved energy levels for an exciton as a function over the knots in ρ-direction can be seen. The exciton in this calculation is in a quantum well with width $\Delta = 1\,\mathrm{nm}$ and the Coulomb potential is replaced by the $1/\rho$-potential. Thus, the Schrödinger equation becomes separable and can be solved analytically. These energy levels therefore should correspond to the energies calculated in equation (2.33) with $n = m = 1$ and $j = 1, 2, \ldots, 12$. It can be seen that after 16 knots the $j = 1, \ldots, 7$ states are quite well converged with an error smaller than 1 m eV. From 24 knots on the states do not change noticeably and for the states with $j = 8, \ldots, 12$ the error remains relatively high. This has something to do with the impact of the not adjusted parameters. The number of knots in z-direction do not matter for the j-states in this potential. Therefore the numerical boundary condition should be adjusted for more accurate solutions. In fact the boundary condition $\Psi(\rho_{\max} = 200\,\mathrm{nm}) = 0$ reduces the error for the $j = 12$ state to less than $0.6\,\mathrm{m\,eV}$. Another effect of increasing the number of knots is the number of possible states for the j-states. That can be explained through the better resolution of the ρ-direction with the B-splines. In the next step

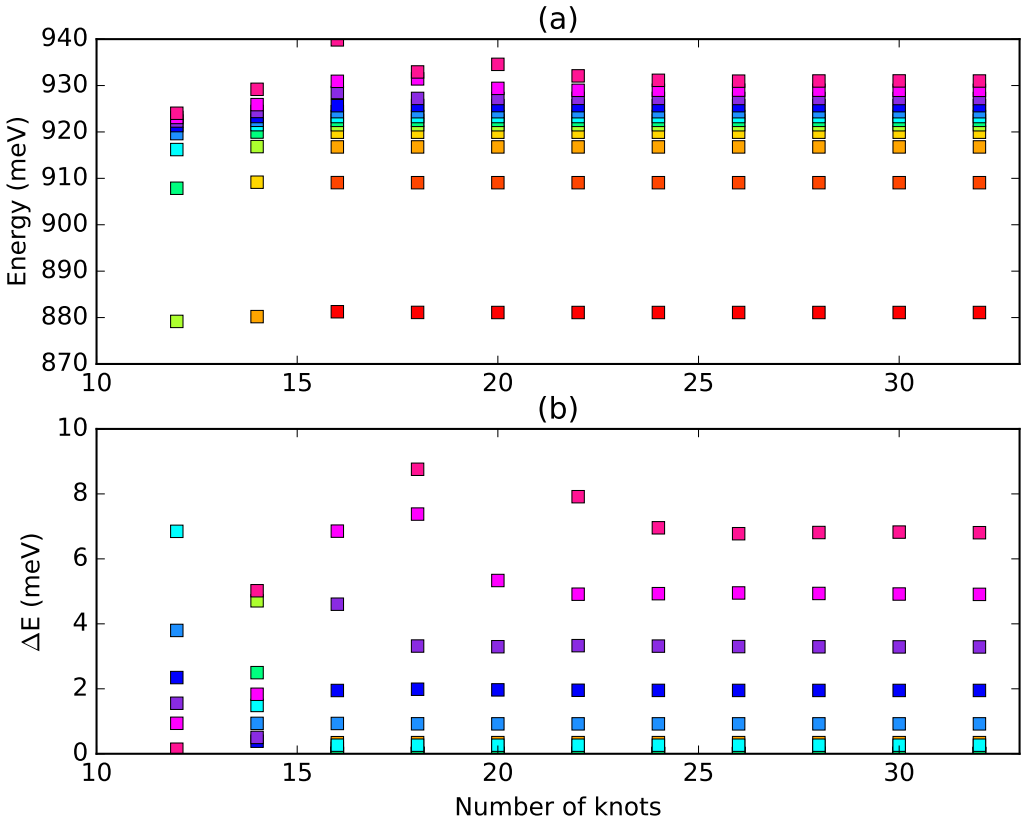

Figure 4.1: In (a) different energy states can be seen over the number of knots in ρ-direction where each color represents an energy state. In (b) the absolute error ΔE in comparison with the analytically calculated energies can be seen. The calculations were done for a quantum well with a width of 1 nm and 12 knots in the z-directions. The numerical boundary condition was $\rho_{\max} = 100\,\text{nm}$, and the order of the B-splines was five.

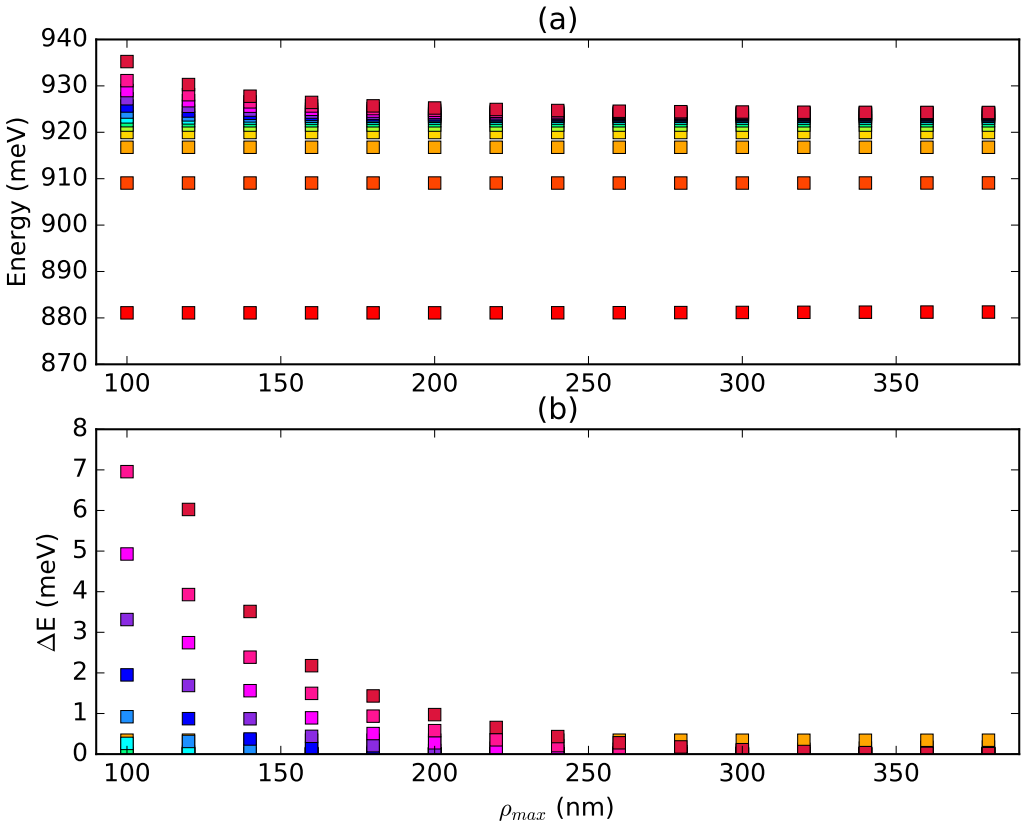

Figure 4.2: In (a) different energy states can be seen over the used $\rho_{\max}$ for the boundary condition $\psi(\rho_{max}) = 0$. In (b) the difference to the analytical calculated values ΔE can be seen. For the calculations 12 knots were used for both z-directions and 24 knots in ρ-direction were used for a quantum well with a width of 1 nm. The order of the B-splines was five.

the convergence in dependency on the numerical boundary condition is investigated. In figure 4.2 the results of this investigation for states up to $j = 13$ can be seen. For higher values of ρ_{max} the numerical calculation converged better. It can be seen that the states with a lower j quantum number already converge for small ρ_{max}. For states with larger j it is important to have a large enough ρ_{max} because otherwise the error becomes large.

4.2 Calculation for different interaction potentials

In this section the results for the $1/\rho$-potential are discussed. In chapter 2 the analytical results have already been discussed. In figure 4.3 some selected states are shown. In this figure the difficulties of the analysis for the different states can be seen, since there are level crossings of the energy states. Therefore those energies need to be carefully assigned to a state. The distance between the red and the green state should be the same for all calculations. The distance should be $32/9\ R_{exc} = 349.59\,\text{meV}$, according to equation (2.33). The error of the numerical calculations can be seen in figure 4.4. Note that the state $(2|1|1)$ did not converge for widths smaller than 0.5 nm. Also a higher deviation for very small widths can be seen. This is probably due to the high energies in this area. Figure 4.4 also shows that the states with $j = 0$ converges slightly worse than the states with $j \geq 1$.

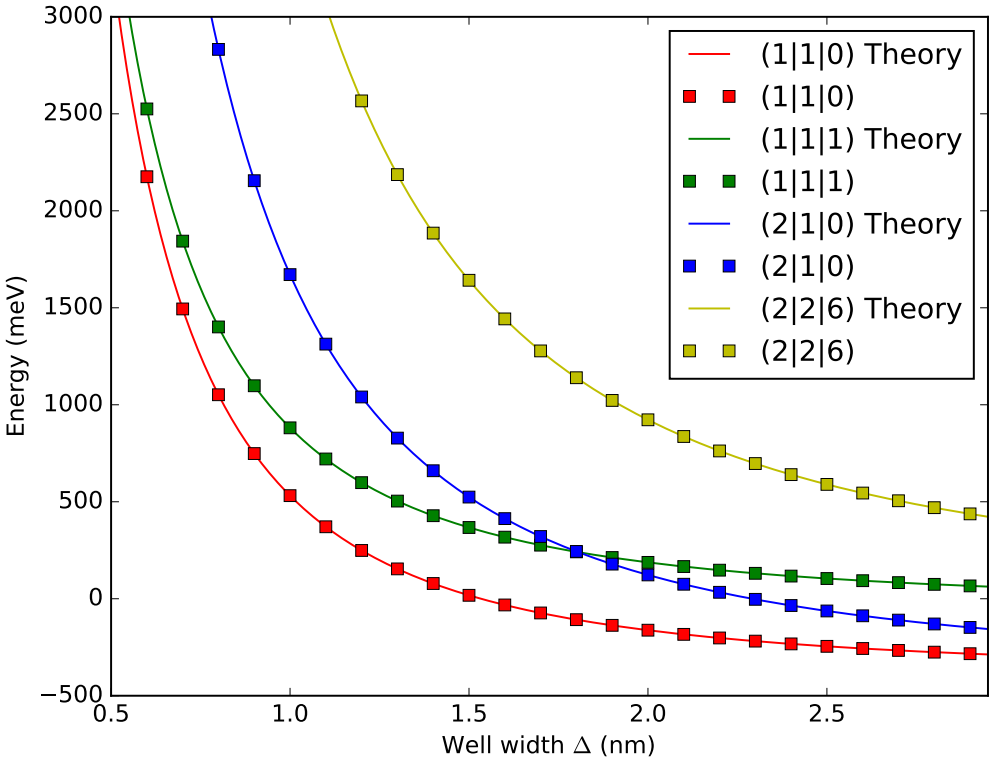

Figure 4.3: Different states with the $1/\rho$-potential can be seen. The states are assigned with $(n|m|j)$ according to equation (2.33). The solid lines represent the analytically calculated values. The used parameters are $\rho_{max} = 100\,\text{nm}$ with 24 knots in ρ-direction.

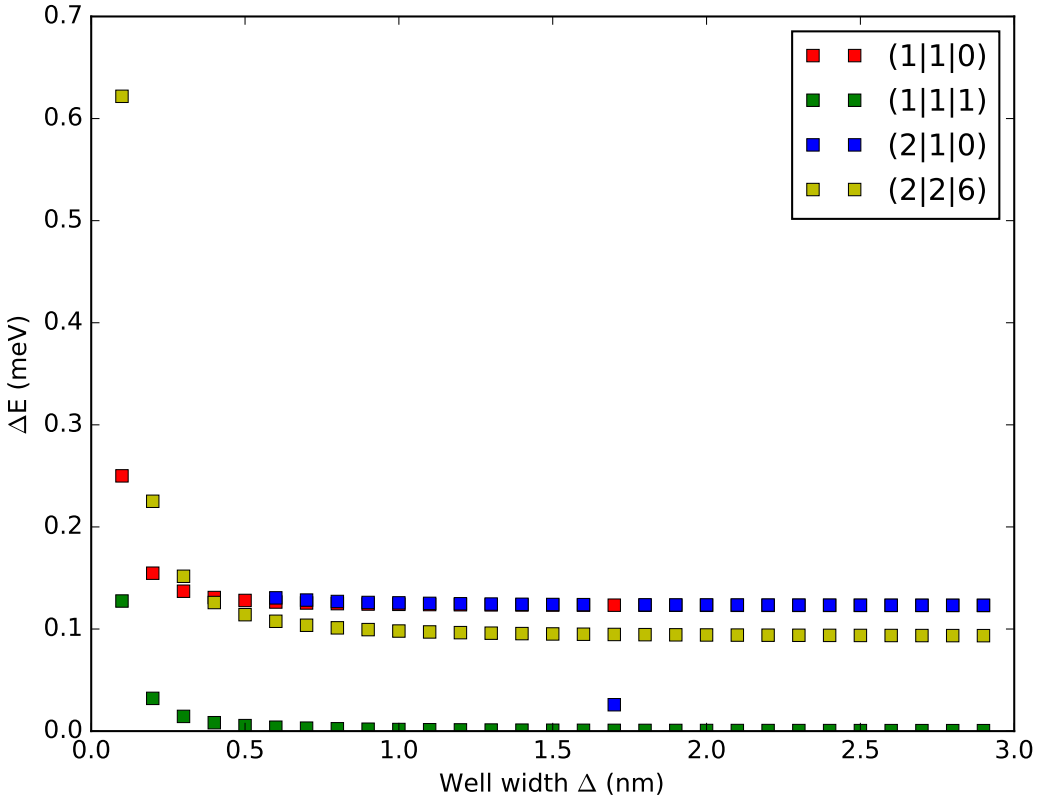

Figure 4.4: The absolute error ΔE for the calculations from figure 4.3 to the analytically expected value is plotted over the quantum well width.

In figure 4.5 the state with the lowest energy for an exciton without Coulomb potential is shown. It can be seen that for widths smaller than 1 nm the energy strongly increases. The energy can be analytically calculated with equation (2.38). The difference is near zero for the calculations with $\geq$14 knots in the z-directions. Here we can see the importance of enough knots in those directions. However the error is relatively low compared to the error that comes with the parameters for ρ that were shown in figure 4.4. The energy of the ρ terms is constant because $\rho_{max} = 200\,\text{nm}$ is constant. If the energies for the quantum wells in the z-directions are subtracted we should get straight lines with constant energy. This also happens as can be seen in Figure 4.6. The convergence is very good for the first nine states. Only for the tenth state we can see noticeable differences.

In figure 4.7 the calculated lowest energy state can be seen for the adiabatic potential, which is given in equation (2.34). For small well widths the energy of the adiabatic

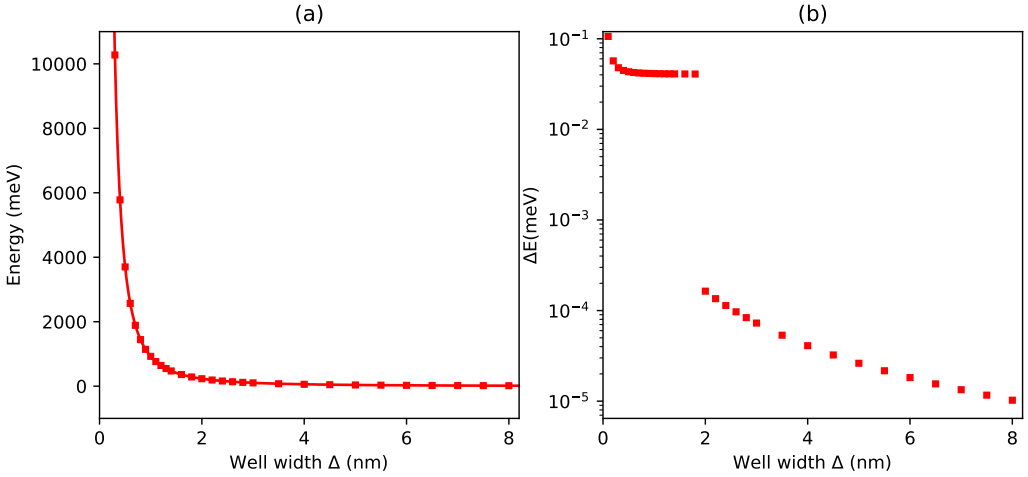

Figure 4.5: On the left the state with the lowest energy for the exciton with heavy hole but without the Coulomb potential is shown over different well widths. On the right side the difference to the analytical result calculated with equation (2.38) is shown. For widths smaller than 2 nm, 12 knots in the z-directions were used. For the widths of 2, 2.2, 2.4, 2.6 and 2.8 nm, 14 knots and for larger widths, 16 knots were used. For the ρ-direction, 24 knots with the boundary condition $\psi(\rho_{max} = 200\,\text{nm}) = 0$ were used.

potential is very low compared to the total energy. It can be seen that the potentialenergy starts at around -350 meV and for wells with width $\Delta = 10$ nm the energy is around -50 meV. As we will see later, this behavior is similar to the Coulomb potential.

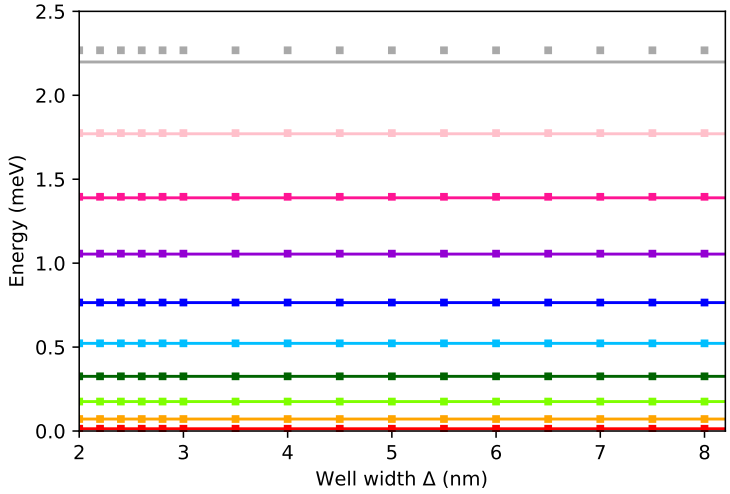

Figure 4.6: The first ten states from the calculation of figure 4.5 with the energy for the z-potentials subtracted. The subtracted energy is calculated with equation (2.30). Each color stands for a state, where the lines are the analytical values and the squares the numerical calculations.

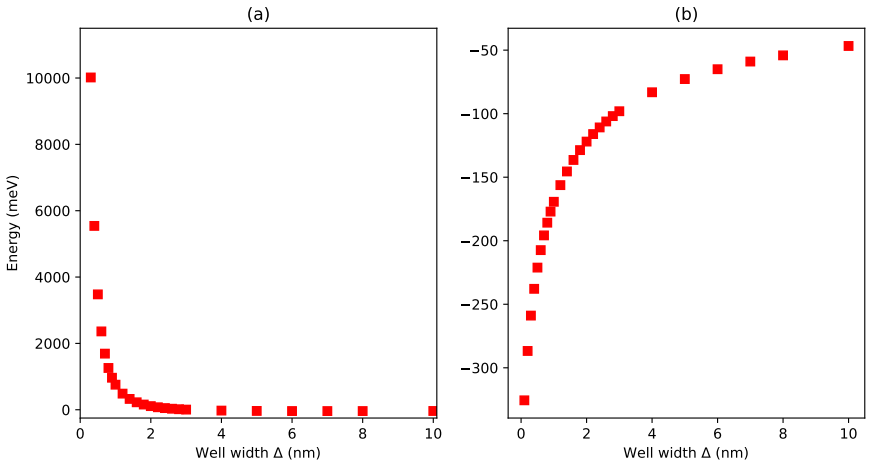

Figure 4.7: The lowest energy for the problem with the adiabatic potential is shown in (a). In (b) the energy with the energy for the quantum well subtracted is shown. The subtracted energy is calculated with equation (2.30). The number of knots in ρ-direction was 24 with the boundary condition at $\rho_{max} = 100\,\text{nm}$. For the z-directions 12 to 20 knots were used.

4.3 Transition from quantum wells to bulk states

The transition from quantum wells to bulk exciton states is to be examined in this thesis. The main focus is on the energy of the Coulomb potential, because this can not be solved analytically. The presumption is that the problem becomes a 2D hydrogen-like problem for very small quantum wells and a 3D hydrogen-like problem for the bulk states, which means that the states correspond to the 3D Rydberg energy. The energies of the quantum wells are subtracted and the remaining energies are compared with the analytical results for the hydrogen-like problems that are given by equation (2.33) for the 2D and equation (2.16) for the 3D problem. This is necessary because for small quantum wells the energy terms that comes from equation (2.30) are dominant. In figure 4.8 one can see the energies of the remaining Coulomb term for small quantum wells until well widths of $\Delta = 3\,\text{nm}$. It can be seen that the energies converge to the 3D model as expected. However it can also be seen that the 2D model is only a good approximation for quantum wells with a smaller width than 0.1 nm. For the first four states the transition looks the same, but for the fifth and sixth state the energy starts between the 2D and 3D Rydberg energy. They only change very little. The expansion of the states can be an explanation for this behavior. However, it may also be that these states are not converged. Another calculation with $\rho_{max} = 380\,\text{nm}$ had the same results. For larger quantum wells the energies can be seen in figure 4.9. There it becomes clear that the lowest state converges exactly to the expected exciton Rydberg energy in three dimensions. The energy of the Coulomb term changes fast for low widths but at $\Delta \approx 3\,\text{nm}$ the energy slowly converges to the exciton Rydberg energy. The whole energy of the exciton becomes lower and also slowly converge to the exciton Rydberg energy since the energy of the quantum well goes to zero for large wells. One can also see that with the change to $\rho_{max} = 380\,\text{nm}$ the energy from the Coulomb term becomes slightly less than for $\rho_{max} = 100\,\text{nm}$. We have to remember that for energies larger than 2980 meV the electron would leave the cuprous oxide. This means that the lowest state is only possible for excitons in a quantum well with width of at least 0.5 nm.

In figure 4.10 the second to the 25th state can be seen. For larger widths of the quantum well the states with higher n and m quantum numbers and with the lowest Coulomb energy are now lower than states with $n = m = 1$ and higher Coulomb energies. This can be observed in the upper left figure. All the other states are now very close together. Note that in this figure also states are included that maybe did not converge and have a little error. For the large scales in the energy however this should not change the course of the states much.

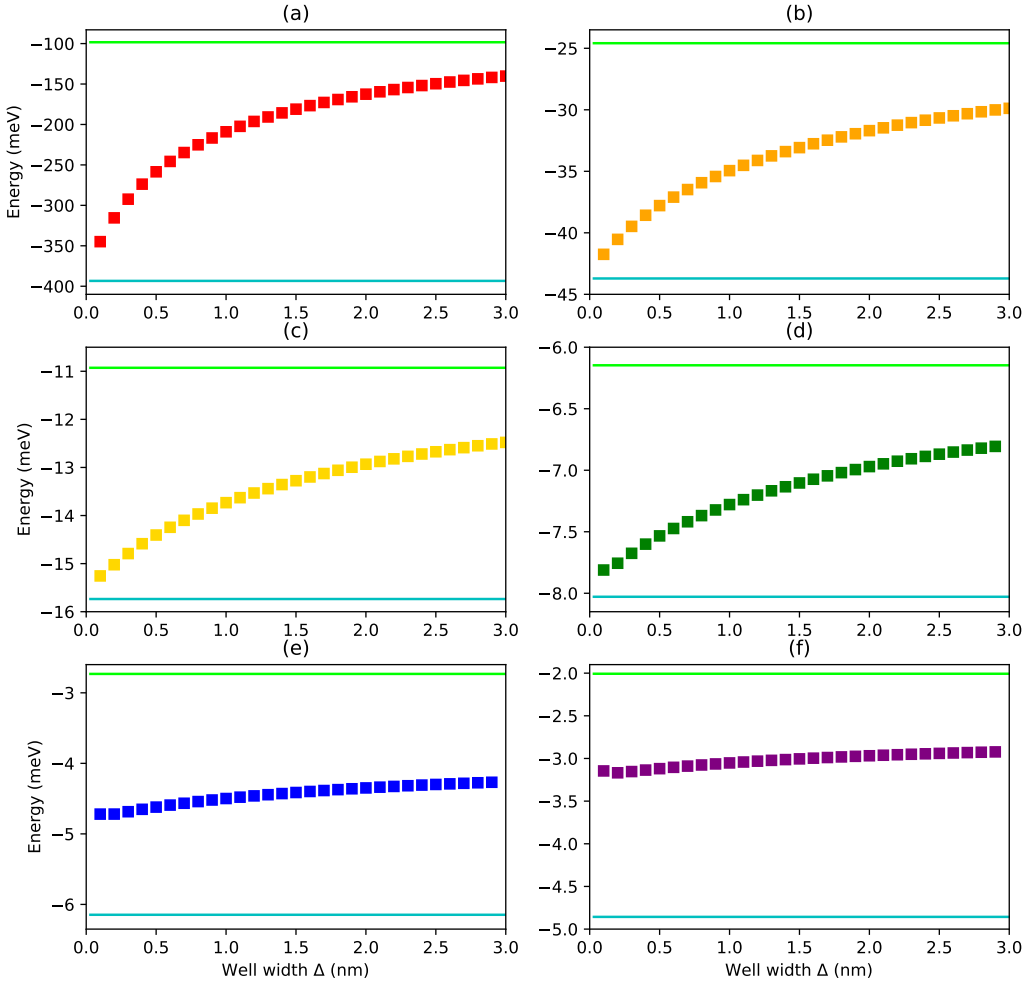

Figure 4.8: The first six states (a, b, c, d, e, f) for excitons with heavy hole over the well width Δ are shown. The green line represents the exciton Rydberg energy in three dimensions and the turquoise line represents the exciton Rydberg energy for two dimensions. The number of knots in z-direction was 10 for the first and went up to 14 for larger widths. The order of the B-splines was 5. For the ρ-direction 24 knots were used and the numerical boundary condition was set to $\rho_{\max} = 100\,\mathrm{nm}$.

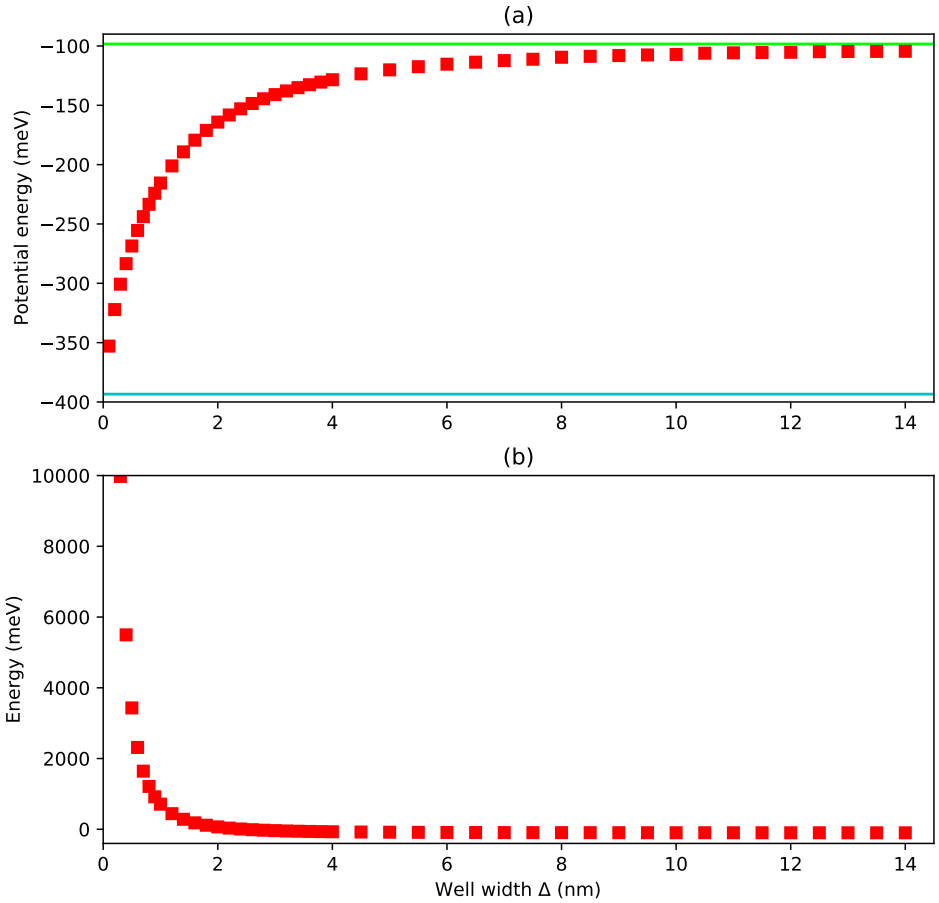

Figure 4.9: In (a) the energies for the lowest exciton state over the widths of the quantum well can be seen. In (b) the analytically calculated energies for the terms of the quantum well are subtracted. The green line represents the exciton Rydberg energy in three dimensions and the turquoise line represents the exciton Rydberg energy for two dimensions. For the ρ-direction 24 knots were used and the numerical boundary condition was set to $\rho_{max} = 380\,\text{nm}$.

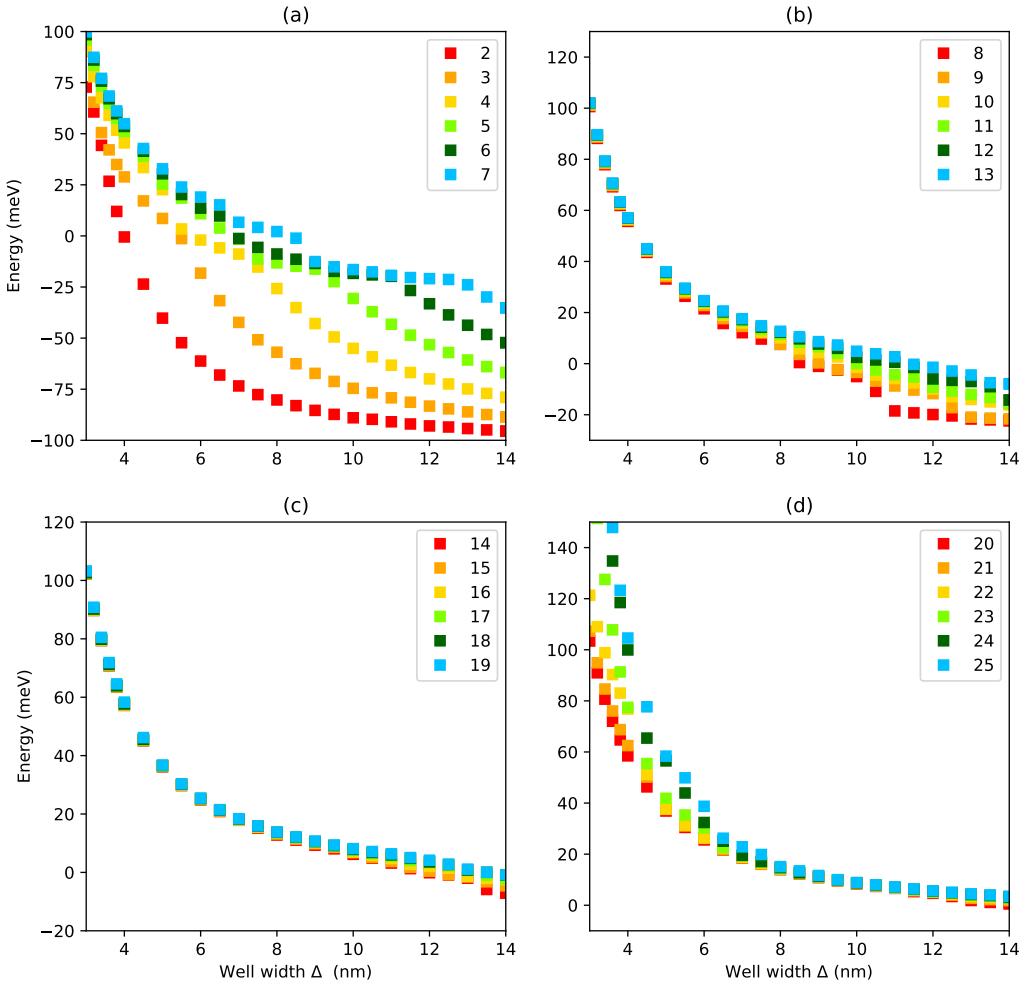

Figure 4.10: Second to the 25th lowest energy states of the exciton over different quantum well widths. For the ρ-direction 24 knots were used and the numerical boundary condition was set to $\rho_{max} = 380\,\text{nm}$.

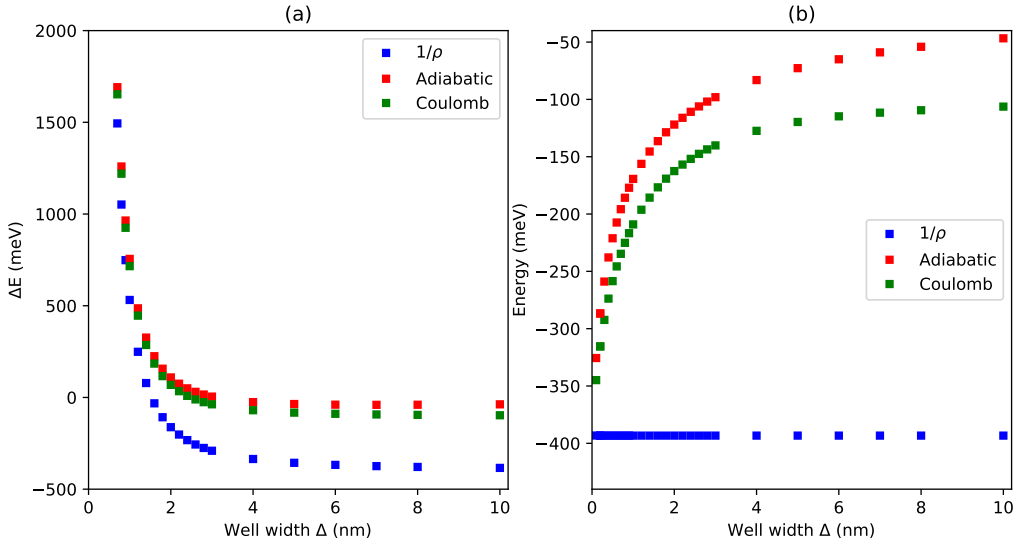

Figure 4.11: (a) The lowest energy state for the $1/\rho$, Coulomb and adiabatic potential over the quantum well width Δ. (b) The with equation (2.30) calculated energy is subtracted. For all potential the boundary condition was $\rho_{\max} = 100\,\text{nm}$. 24 knots were used in ρ-direction and 12-20 knots in the z-directions.

In figure 4.11 the lowest energy state for three different interaction potentials is shown. One can see that the adiabatic potential is a good approximation of the Coulomb potential for $\Delta \leq 1\,\text{nm}$. The advantage of the adiabatic potential is that with the right implementation the computation time is faster than for the Coulomb potential. Since the adiabatic potential converges to the $1/\rho$-potential for large ρ, for different boundary conditions and states with higher energy that are more expanded the energy can look different. It can be seen that the $1/\rho$-potential remains the same for different well with since it is independent of z_e and z_h.

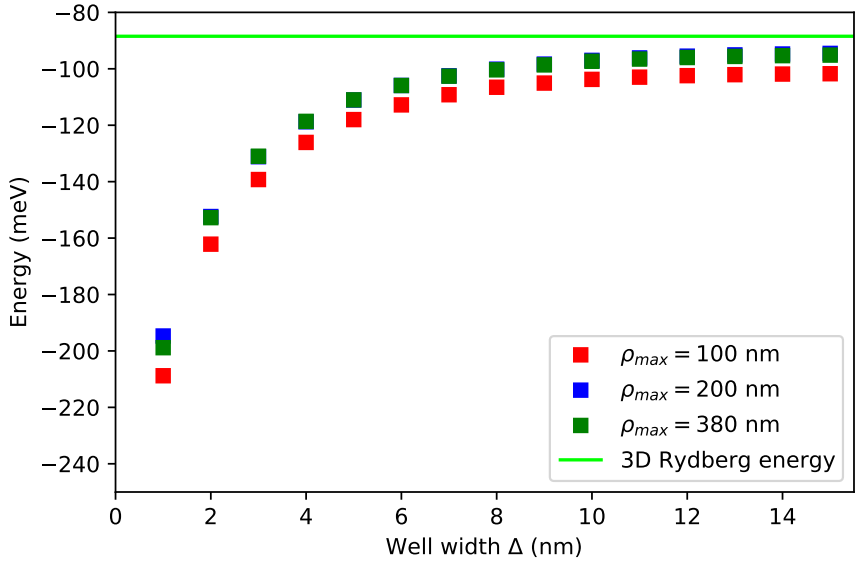

Figure 4.12: Energy with the energy for the quantum well subtracted over the well width for different numerical boundary conditions. The calculation was done for the light hole and the green line represents the exciton Rydberg energy in three dimensions. The number of knots in ρ -direction was 24 and in the z-directions at least twice as many knots as the width in nanometers were used. The blue and green squares are overlapping except for the width of 1 nm.

For the light hole the lowest energy for each quantum well width can be seen in figure 4.12. One can see that the states converge not as well as the states for the heavy hole to the calculated exciton Rydberg energy. For $\rho_{max} = 100\,\text{nm}$ the energy states are further away from the expected values but for larger ρ_{max} the convergence is significantly better. It needs further investigations for which parameters the energy will converge to the Rydberg energy.

5 Summary and outlook

In this thesis the transition from quantum wells to bulk exciton states in cuprous oxide was investigated. For the numerical computation B-spline basis functions were used. The convergence of eigenvalues for different potentials was investigated by comparing the numerical results with the analytical results. It was shown that the number of knots in ρ-direction and the numerical boundary condition have a huge influence on the number of converged states. For the $1/\rho$-potential it was shown that the computation yield good values with small error. Without a potential the first nine states converged almost exactly for calculations with 24 knots in ρ-direction. In the next step the transition from quantum well to bulk exciton states was done. It was discovered that already for quantum wells with a width of around 10 nm the lowest state is in a bulk state. For states with higher energy, bulk states are only approached for broader quantum wells. The first four states proceed as expected and went from the 2D Rydberg energy to the 3D Rydberg energy. The transition was faster for well widths smaller than 1 nm and then slowly converges to the 3D Rydberg energy. For states with higher order the energy was nearly constant. For larger quantum wells the Coulomb term becomes dominant and states with higher quantum numbers n and m are now between the first and second lowest state with quantum numbers $n = 1$ and $m = 1$. Further, the states become very close to another for larger quantum wells. The computation for the light hole which represents the other valence band was also done. Overall the usefulness and the accuracy of using B-splines for the computation could be demonstrated and the transition from quantum well to bulk exciton states could be calculated.

The next steps could be the optimisation of the calculation of the eigenvalues. There are many different routines in the LAPACK library that can be used and also take the banded structure of the B-spline matrix into account. Another step would be the implementation of the correction terms for the band structure of cuprous oxide and the central-cell corrections. Another step would be the writing of a program that identifies the different states with their associated quantum numbers. This would benefit the evaluation of the data.

6 Zusammenfassung in deutscher Sprache

In dieser Arbeit wurden die Energien der Zustände von Exzitonen in Kupferoxydul untersucht, welche sich in einem Potentialtopf in z-Richtung befinden. Für die numerische Berechnung wurden B-Spline Funktionen verwendet um die Wellenfunktion zu approximieren. Um die Konvergenz des Programms zu testen wurden zunächst analytisch lösbare Probleme berechnet. Dafür wurde das Coulombpotential zum einen weggelassen und zum anderen durch andere Potentiale ersetzt, nämlich ein $1/\rho$- und ein adiabatisches Potential. Dadurch konnten die berechneten Werte verglichen werden und es zeigte sich, dass die Zahl der Knoten, so wie die numerische Randbedingung wesentlich für die Konvergenz der Zustände sind. Diese Beeinflussen zum einen die Genauigkeit der berechneten Werte und ebenfalls die Anzahl der konvergierten Zustände. Auch wurde gezeigt, dass für Ergebnise, welche einen absoluten Fehler von weniger als 10^{-3} meV haben sollen mindestens 14 Knoten in die z-Richtungen benötigt werden. Der Fokus dieser Arbeit lag auf der Untersuchung des Verhaltens der Zustände für verschiedene Breiten des Potentialtopfes in z-Richtung. Für den energetisch niedrigsten Zustand konnte gezeigt werden, dass bereits für Potentialtöpfe mit Breiten von um die 10 nm der Zustand sich wie ein Zustand in Kupferoxydul ohne Potentialtopf verhält. Für sehr kleine Potentialtöpfe nährte sich die Energie des Coulombtherms der zweidimensionalen Exziton Rydbergenergie an. Dies konnte für die ersten vier Zustände gezeigt werden. Die Zustände darüber verhielten sich anders, was daran liegen könnte, dass diese nicht konvergiert sind. Dies bedarf noch einer genaueren Untersuchung. Des weiteren konnte gezeigt werden, dass für größere Potentialtöpfe der Teil der Energie, die aus dem Coulombterm resultiert, dominant ist. Für Exzitonen mit dem leichteren Loch, welches ein anderes Valenzband repräsentiert, konnte ähnliches Verhalten festgestellt werde. Jedoch konvergieren die Energien nicht so gut gegen die dreidimensionale Rydbergenergie wie beim schweren Loch. Zusammenfassend konnte mit Hilfe der B-Spline Funktionen die Energiezustände der Exzitonen in verschieden breiten Potentialtöpfen untersucht werden und ein tieferes Verständnis für das Verhalten von Exzitonen erlangt werden.

Bibliography

[1] G. H. Wannier. "The structure of electronic excitation levels in insulating crystal". In: *Phys. Rev.* 52.191 (1937). DOI: https://doi.org/10.1103/PhysRev.52.191.

[2] T. Kazimierczuk, D. Fröhlich, S. Scheel, H. Stolz, and M. Bayer. "Giant Rydberg excitons in the copper oxide Cu_2O". In: *Nature* 514.7522 (Oct. 2014), pp. 343–347. ISSN: 0028-0836. DOI: 10.1038/nature13832.

[3] Frank Schweiner. "Theory of excitons in cuprous oxide". PhD thesis. 2017. DOI: 10.18419/opus-9483.

[4] Bruce W. Shore. "Solving the radial Schrödinger equation by using cubic-spline basis functions". In: *The Journal of Chemical Physics* 58.9 (1973), pp. 3855–3866. DOI: 10.1063/1.1679740. eprint: https://doi.org/10.1063/1.1679740. URL: https://doi.org/10.1063/1.1679740.

[5] Siegfried Hunklinger and Christian Enss. *Solid State Physics*. De Gruyter, Berlin, 2022. ISBN: 978-3-11-066645-8.

[6] E. Wigner and F. Seitz. "On the Constitution of Metallic Sodium". In: *Phys. Rev.* 43 (10 1933), pp. 804–810. DOI: 10.1103/PhysRev.43.804. URL: https://link.aps.org/doi/10.1103/PhysRev.43.804.

[7] Rudolf Gross and Achim Marx. *Festkörperphysik*. Oldenbourg Wissenschaftsverlag, München, 2012. ISBN: 9783486714869. DOI: doi:10.1524/9783486714869. URL: https://doi.org/10.1524/9783486714869.

[8] J. M. Luttinger and W. Kohn. "Motion of Electrons and Holes in Perturbed Periodic Fields". In: *Phys. Rev.* 97 (4 Feb. 1955), pp. 869–883. DOI: 10.1103/PhysRev.97.869. URL: https://link.aps.org/doi/10.1103/PhysRev.97.869.

[9] Ulrich Rössler. *Solid State Theory: An Introduction*. Springer Berlin, Heidelberg, 2012. ISBN: 9783540927624. URL: http://dx.doi.org/10.1007/978-3-540-92762-4.

[10] Annika Konzelmann, Bettina Frank, and Harald Giessen. "Quantum confined Rydberg excitons in reduced dimensions". In: *Journal of Physics B: Atomic, Molecular and Optical Physics* 53.2 (Dec. 2019), p. 024001. DOI: 10.1088/1361-6455/ab56a9. URL: https://doi.org/10.1088/1361-6455/ab56a9.

[11] Michael Jörger. "Terahertzspektroskopie an Cu2O: Intraexzitonische und phononische Übergänge". PhD thesis. 2004. ISBN: 3-86537-244-9.

[12] Patrik Zielinski. *Berechnung hochangeregter Exzitonen in elektrischen und magnetischen Feldern mit der Methode der komplexen Koordinatenrotation*. Masterthesis, Universität Stuttgart, 2018. DOI: 10.18419/opus-10130.

[13] J. W. Hodby, T. E. Jenkins, C. Schwab, H. Tamura, and D. Trivich. "Cyclotron resonance of electrons and of holes in cuprous oxide, Cu_2O". In: *Journal of Physics C: Solid State Physics* 9.8 (1976), p. 1429. DOI: 10.1088/0022-3719/9/8/014.

[14] O. Madelung, U. Rössler, and M. Schulz, eds. *Cuprous oxide (Cu2O) dielectric constant: Datasheet from Landolt-Börnstein - Group III Condensed Matter · Volume 41C: "Non-Tetrahedrally Bonded Elements and Binary Compounds I" in SpringerMaterials (https://doi.org/10.1007/10681727_58)*. Copyright 1998 Springer-Verlag Berlin Heidelberg. DOI: 10.1007/10681727_58. URL: https://materials.springer.com/lb/docs/sm_lbs_978-3-540-31360-1_58.

[15] M. E. Portnoia D. G. W. Parfitt. "The two-dimensional hydrogen atom revisited". In: *Zeitschrift für Physikalische Chemie* 43.10 (2002). DOI: 10.1063/1.1503868.

[16] M. Paluszny H. Prautzsch W. Boehm. *Bézier and B-Spline Techniques*. Springer Berlin, Heidelberg, 2002, pp. 59–65. DOI: https://doi.org/10.1007/978-3-662-04919-8.

[17] Carl De Boor, ed. *A practical guide to splines*. Englisch. Rev. ed., 1. hardcover print. New York ; Heidelberg: Springer, 2001. ISBN: 9780387953663.

[18] Pavel A. Belov. "Linewidths and energy shifts of electron-impurity resonant states in quantum wells with infinite barriers". In: *Phys. Rev. B* 105 (15 Apr. 2022), p. 155417. DOI: 10.1103/PhysRevB.105.155417. URL: https://link.aps.org/doi/10.1103/PhysRevB.105.155417.

[19] E. Anderson, Z. Bai, C. Bischof, S. Blackford, J. Demmel, J. Dongarra, J. D. Croz, A. Greenbaum, S. Hammarling, and A. McKenney. *LAPACK Users' Guide, Third edition*. Society for Industrial and Applied Mathematics, Philadelphia, 1999.

Danksagung

An dieser Stelle möchte ich allen danken, die mich bei dieser Arbeit unterstützt haben. Ein besonder Dank gilt dabei Jörg Main der sich viel Zeit für mich genommen hat und der die Arbeit erst möglich machte. Des Weiteren danke ich Patric Rommel und Jan Ertl die mich im Verlauf der Arbeit stets gut betreut haben. Ebenfalls bedanke ich mich bei Pavel Belov das Programm zu Verfügung stellte und der mir bei Fragen immer zur Seite stand. Ich bedanke mich auch bei allen anderen Mitgliedern des 1. Instituts für Theoretische Physik für die angenehme Atmosphäre und die interessanten Gespräche.

Erklärung

Ich versichere,

- dass ich diese Bachelorarbeit selbstständig verfasst habe,
- dass ich keine anderen als die angegebenen Quellen benutzt und alle wörtlich oder sinngemäß aus anderen Werken übernommenen Aussagen als solche gekennzeichnet habe,
- dass die eingereichte Arbeit weder vollständig noch in wesentlichen Teilen Gegenstand eines anderen Prüfungsverfahrens gewesen ist,
- und dass das elektronische Exemplar mit den anderen Exemplaren übereinstimmt.

Stuttgart, den 9. September 2022 *Leon Kühner*